JOURNAL OF GEOPHYSICAL RESEARCH, VOL. 106, NO. C2, PAGES 2743–2759, FEBRUARY 15, 2001

Antarctic Circumpolar Current response to zonally averaged winds

Sarah T. Gille,[1] David P. Stevens,[2] Robin T. Tokmakian,[3] and Karen J. Heywood[4]

Abstract. Coherence analysis techniques are used to compare Southern Ocean wind forcing with Antarctic Circumpolar Current transport. Winds are derived from five different products: ERS winds that have been bin-averaged, weekly gridded ERS winds produced by the Centre ERS d'Archivage et de Traitement, 5 day winds from the Special Sensor Microwave Imager, analysis winds from the European Centre for Medium-Range Weather Forecasts, and reanalysis winds from the National Centers for Environmental Prediction. Barotropic transport is estimated from the pressure difference between bottom pressure gauges deployed on either side of Drake Passage by Proudman Oceanographic Laboratory as part of the World Ocean Circulation Experiment. Surface transport is estimated from TOPEX altimetry. Results indicate that transport and wind forcing are coherent over a broad range of frequencies, corresponding to time periods of roughly 10–256 days. Highest coherences occur for winds at latitudes on the south side of Drake Passage. Barotropic ocean transport lags wind forcing not by a constant time interval but by a constant phase lag of about one eighteenth of a cycle at a broad range of frequencies, suggesting that the oceanic response to wind is controlled by both the tendency term and a frequency-dependent viscous process. Surface transport lags by a longer phase interval. Wind stress curl north of Drake Passage is more coherent with transport than is wind stress curl in the latitudes of Drake Passage. Ocean transport lags wind stress curl, suggesting that transport fluctuations are not governed by a simple Sverdrupian vorticity balance. Like the observations, general circulation model transports from the Parallel Ocean Program and from the Parallel Ocean Climate Model are coherent with wind stress from the south side of Drake Passage and with wind stress curl from latitudes north of Drake Passage. Unlike the observations, model transport and bottom pressure vary almost simultaneously with the wind and do not replicate the observed phase lags, implying that the effective model viscosity may be too large.

1. Introduction

The strongest winds in the world blow over the Southern Ocean. Reanalysis fields from the European Centre for Medium Range Weather Forecasts (ECMWF) [*Trenberth et al.*, 1989] indicate that the time-averaged zonal wind stress through Drake Passage (60°W; 54°–60°S) is about a factor of 3 larger than midlatitude winds, with a value between 0.08 and 0.09 N m^{-2}. *Wunsch* [1998] estimated that the Southern Ocean receives 70% of the work done by the wind on the ocean. These powerful winds are responsible for driving the Antarctic Circumpolar Current (ACC) which is estimated to carry an average transport of 134×10^6 $m^3 s^{-1}$ [*Nowlin and Klinck*, 1986].

In addition to being strong, Southern Ocean winds are also highly variable. ECMWF fields in Drake Passage have a standard deviation between 0.13 and 0.14 N m^{-2}, ~50% greater than the mean wind stress. This wind variability is assumed to be responsible for observed 5–10 Sv root mean squared variations in the strength of ACC transport [*Whitworth and Peterson*, 1985; *Meredith et al.*, 1996]. Studies based on meteorological analysis winds and Drake Passage transport estimates have consistently found that fluctuations in wind stress are correlated with fluctuations in ACC transport, with wind leading transport by small time periods. Table 1 summarizes the findings of these investigations, which have variously estimated the lag between wind and transport to be anywhere between a fraction of a day and 17 days. However, the details of Southern Hemisphere wind fields from model output have been considered somewhat suspect: for the time period between July and September 1978, *Mestas-Nuñez et al.* [1994] found that the ECMWF model did not reliably reproduce the Southern Ocean winds seen by the Seasat scatterometer.

This study revisits the question of Southern Ocean variability in response to wind, using satellite wind products in addition to meteorological fields from ECMWF and from the National Centers for Environmental Prediction (NCEP). These are compared with transport estimates derived from a

[1] Department of Earth System Science, University of California, Irvine.
[2] School of Mathematics, University of East Anglia, Norwich, England, United Kingdom.
[3] Naval Postgraduate School, Monterey, California.
[4] School of Environmental Sciences, University of East Anglia, Norwich, England, United Kingdom.

Paper number 1999JC900333
0148-0227/01/1999JC900333$09.00

Table 1. Results of Previous Investigations Comparing Drake Passage Transport Estimates With Wind Forcing

Study	Wind Product	Ocean Instruments	Duration	Significant Coherence	Reported Lag
Wearn and Baker [1980] (hereinafter referred to as WB80)	geostrophic, sea level atmospheric pressure from Australian Bureau of Meteorology	north–south BPRs (500 m)	2.5 years (1976-1978)	5–50 days	9.5 days[a] (<1 day for periods < 10 days)
Whitworth [1983]	same as WB80	current meters, pressure recorders, thermistors (surface to 2500 m)	370 days (1979)	16–24 days	17 days
Peterson [1988]	same as WB80	north–south BPRs (500 m)	4 years (1976-1979)	75–220 days	14 days
Hughes et al. [1999]	ECMWF	south BPR (1000–4000 m at three locations)	5 years (1989-1994)	15–45 days; 60–220 days	near zero
this study	ECMWF; NCEP; SSM/I; CERSAT; ERS-1; ERS-2	north–south BPRs (1000 m) (fixed locations)	5 years (1992-1997)	10–256 days see text, Plates 1a,2a	1/18th cycle see text, Plates 1b,2b

All but the present study have relied on meteorological analysis winds. The wind products used in this study are discussed in section 3.
[a]Based on lagged correlations. *Chelton* [1982] noted that wind and ocean signals with strong annual cycles may appear coherent, even if they are not causally related, and as a result, subsequent studies have focused primarily on coherence analysis.

5 year time series of Drake Passage bottom pressure data collected by Proudman Oceanographic Laboratories and from TOPEX altimeter measurements of surface velocity variability for the entire Southern Ocean. As a byproduct of examining the ocean's response to wind, we also provide a comparison of five different wind products available over the global ocean for an extended time period during the early 1990s, overlapping with much of the World Ocean Circulation Experiment (WOCE) observational work, and we evaluate how well global ocean general circulation models duplicate the observed characteristics of ocean response to wind.

Section 2 discusses ways in which the ACC might be expected to respond to wind forcing. Section 3 describes the measurements used in this study. Section 4 shows the correlations and coherences between the winds and bottom pressure recorder (BPR) proxies for ACC transport. Section 5 shows how these results compare with findings from two different ocean general circulation models. Finally, section 6 summarizes the results.

2. Wind Stress and Transport in the Equations of Motion

The mechanisms by which winds drive the ACC have been the subject of extensive debate. Attention has focused primarily on the physics governing the mean flow. *Munk and Palmén* [1951] first suggested that surface wind stress over the ACC might be balanced by form stress due to pressure gradients across topographic obstructions on the ocean floor. The momentum balances in numerical models of the Southern Ocean are consistent with wind stress balancing form stress [*Stevens and Ivchenko*, 1997; *Gille*, 1997], but in their simplest form these equations do not account for the size of the mean ACC itself. *Johnson and Bryden* [1989] suggested that the size of the ACC should be controlled by the baroclinic instability required to transfer momentum vertically from where it is inserted at the surface to where it is removed at the bottom.

Stommel [1957] proposed that the transport of the ACC can be explained by invoking a Sverdrup balance in which wind stress curl input at the surface removes vorticity from the current, driving it in a southward spiral around the Antarctic continent. Topographic obstructions at Drake Passage act as a western boundary, allowing vorticity input to the ACC and northward flow. *Baker* [1982] showed that such a balance was consistent with the structure and magnitude of the mean winds over the Southern Ocean. On the basis of heat budget arguments, *Warren et al.* [1996] also suggested that the ACC is in Sverdrup balance, though their points have inspired ongoing discussion [*Hughes*, 1997; *Warren et al.*, 1997; *Olbers*, 1998; *Warren et al.*, 1998].

More recent studies based on numerical models have suggested that in addition to wind stress and wind stress curl, buoyancy forcing may also play a role in determining ACC transport [*Gnanadesikan and Hallberg*, 2000; *Gent et al.*, 2000]. Other studies have pointed to the importance of topography [e.g., *Völker*, 1999] and the coupling between wind stress and thermohaline forcing [*Cai and Baines*, 1996].

Available data are inadequate to provide definitive explanations for the dynamical processes controlling the mean flow of the ACC: study of the mean ACC requires knowing not only the mean transport but also how it would differ under alternative oceanic conditions. Observations instead allow us to examine how transport fluctuates in response to changes in forcing. In some frequency ranges we might expect that these responses could be analogous. For example, *Stammer* [1997b] found that the time-dependent components of circulation in the North Pacific were consistent with a

Sverdrup balance. This study therefore focuses on variability of the ACC.

To understand how the ACC responds to wind, first consider the zonal equation of motion,

$$u_t+uu_x+vu_y+wu_z-fv=-\frac{1}{\rho_o}\frac{\partial p}{\partial x}+\frac{\partial}{\partial z}\left[\frac{\tau_x}{\rho_o}\right]-bu+\nu\nabla^2 u, \tag{1}$$

where u and v represent velocities in the x and y directions, f is the Coriolis parameter, ρ_o is the background density, p is pressure, ν is viscosity, and b represents the linear drag term, which is unconventional but helpful for thinking about the physics of the ACC. The ACC is not zonal but instead is steered on a meandering path around bathymetry so that unforced barotropic flow should follow contours of f/H [e.g., *Marshall*, 1995; *Hughes et al.*, 1999]. If we neglect the curvature terms associated with the meandering of the ACC, then (1) can be interpreted to represent the flow in stream coordinates, where u is the along-stream velocity and v the cross-stream velocity.

Averaged vertically and along stream and linearized, the momentum equation can be approximated:

$$U_t + R_y = F + \left[\frac{\overline{\tau^x}}{H\rho_o}\right] - bU + \nu\nabla^2 U, \tag{2}$$

where x and y represent the along-stream and cross-stream directions, respectively; U is the vertically and along-stream averaged velocity; R is the vertically and along-stream averaged product of u and v; H is a measure of depth; and F is form stress due to the net pressure gradient induced by seafloor topography. The averaged meridional velocity V is expected to be near zero, and R is not readily represented as a linearized quantity. The omitted wu_z term may also influence the momentum balance significantly, so (2) should be thought of as a cartoon.

Form stress F relies on eddy fluxes to transmit momentum vertically through the water column to the depths at which topography can establish net pressure gradients [*Johnson and Bryden*, 1989]. Since the measurements available in this study are at the ocean surface (altimetry) and at 1000 m depth (bottom pressure), F is likely to be best represented by the nonlinear terms in the momentum balance rather than by the poorly known deep ocean pressure gradients. In addition, form stress is not necessarily directly linked to transport [*Warren et al.*, 1996], particularly on the timescales resolved in this analysis. For these reasons this analysis will not explore the relationship between F and wind stress explicitly.

The frequency domain provides a natural framework for examining ocean response to wind fluctuations. Fourier transforming equation (2) produces

$$-i\omega\hat{U} + \hat{R}_y = \hat{F} + \hat{\tau} - b\hat{U} + \nu\nabla^2\hat{U}, \tag{3}$$

where a circumflex indicates the Fourier transform and $\hat{\tau}$ is the Fourier transform of $\tau^x/\rho_o H$.

For comparison, the Fourier transform of the linearized vorticity equation that defines the Sverdrup balance states

$$-i\omega\hat{\zeta} + \beta\hat{V} = \mathrm{curl}\hat{\tau} - b\hat{\zeta} + \nu\nabla^2\hat{\zeta}, \tag{4}$$

where ζ represents zonally and vertically averaged relative vorticity, and nonlinear and bottom drag terms have been neglected.

The statistical analysis of wind stress and ACC transport data in this paper will focus on coherence. This will allow us to evaluate not only how closely the wind and transport time series match at a broad range of frequencies but also the phase lag between wind and transport. Coherence is defined as

$$C = \left|\frac{<\hat{\tau}\hat{U}^*>}{\sqrt{<\hat{\tau}\hat{\tau}^*><\hat{U}\hat{U}^*>}}\right|, \tag{5}$$

where asterisks denote the complex conjugate and brackets denote the mean of multiple realizations. High coherences C indicate that the signals have a consistent relationship, although their peaks may come at different points in time. Low coherence indicates that the signals have a random relationship to each other. The phase lag between the two signals is

$$\phi = \mathrm{atan}\left[\Im(<\hat{\tau}\hat{U}^*>)/\Re(<\hat{\tau}\hat{U}^*>)\right], \tag{6}$$

where the signs of the numerator and denominator are used to insure that ϕ has a range from $-\pi$ to π radians.

Variations in wind stress should be balanced by compensating variations in one or more of the other terms in the momentum balance. Several scenarios are possible.

1. If the tendency term U_t balances wind stress fluctuations, then $-i\omega\hat{U} \approx \hat{\tau}$. The phase lag between wind and ACC transport is therefore

$$\phi = \mathrm{atan}(-\omega/0) = -\frac{\pi}{2}, \tag{7}$$

so that transport lags wind stress by a quarter cycle.

2. In contrast, if the dominant process balancing wind stress comes from the linear drag term or a frictional term, there is no simple way to introduce a phase lag between wind stress and ACC transport into these simplified barotropic equations. The phase lag is expected to be of the form

$$\phi = \mathrm{atan}(0/1) = 0. \tag{8}$$

The Laplacian operator ∇^2 may mean that the spatial location of maximum transport is shifted relative to the location of maximum wind, but there can be no temporal lag.

3. If the nonlinear terms dominate the response, so that $\hat{R}_y \approx \hat{\tau}$, then τ and U could have entirely different spectra, and the coherence between the two signals at any given frequency may be negligibly small.

4. Finally, if the ACC responds more strongly to wind stress curl than to wind stress, we might see evidence that $\beta\hat{V} \approx \mathrm{curl}\hat{\tau}$. If the ocean reaches this equilibrium Sverdrup balance instantly, then there would be no phase lag between τ and the ACC transport V, as in the case of frictional response to wind. If the wind drives forced Rossby waves, a zonal mean forcing $\mathrm{curl}\tau = \cos(\omega t - ly)$ will lead to a stream function of the form $\sin(\omega t - ly)$, and in turn, a zonal velocity in phase with the wind and a meridional velocity of zero. In the zonal mean therefore we expect no lag between wind stress curl and ocean response. The details of the vorticity balance are not so simple, and the additional

terms in the balance might result in a phase lag. However, for this study, insufficient observations are available to make any statements about $\hat{\zeta}$.

Thus, only the tendency term balance $U_t \approx \tau^x$ is likely to produce a phase lag between wind stress and ocean transport. In reality we expect that the true ocean's response to zonally averaged wind will represent a combination of these physical processes (and that time-varying ocean transports will also be influenced by a variety of other factors including buoyancy forcing, topography, and baroclinic instability). *Wearn and Baker* [1980] derived an analytic solution to (2) for the case in which R, F, and ν are all zero, and wind is balanced simply by a tendency term and a linear drag term. In this case, if the wind stress is $\tau_o e^{i\omega t}$, then

$$U(t) = \frac{\tau_o}{\sqrt{b^2 + \omega^2}} e^{i(\omega t - \phi)}, \tag{9}$$

where

$$\phi = \text{atan}(-\omega/b). \tag{10}$$

The observed lag ϕ provides a framework for evaluating the relative importance of the tendency term compared with other terms in the analysis that follows.

3. Data

3.1. Bottom Pressure

As part of WOCE, Proudman Oceanographic Laboratory's Antarctic Circumpolar Current Levels by Altimetry and Island Measurements (ACCLAIM) program has deployed BPRs in various positions in the Drake Passage area since 1989 [*Meredith et al.*, 1996; *Hughes et al.*, 1999; *Gille*, 1999]. This study will focus on two BPRs identified by stars in Figure 1, located at either end of the WOCE SR1b repeat line. These BPRs were deployed starting in November 1992, and this analysis will consider the record through November 1997. Data were ordinarily recovered annually, although the recorders deployed in 1994 were not picked up until 1996. Measurements were archived at 15 min or hourly intervals, filtered to minimize semidiurnal and diurnal tidal aliasing, and subsampled at 12 hour intervals. Data may also contain tidal energy at fortnightly and monthly intervals that has not been removed. For this analysis, demeaned records from consecutive BPR deployments were concatenated to generate an extended time series. Since mean pressure could experience interannual variability, minor adjustments were allowed to minimize pressure differences between the end of one record and the start of the next.

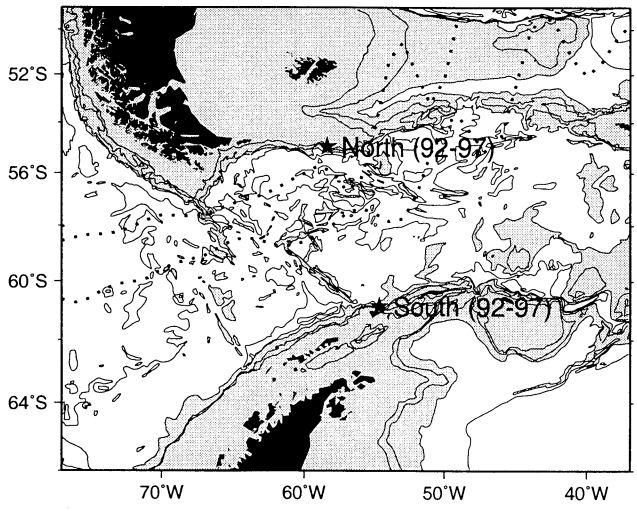

Figure 1. Locations of bottom pressure gauges used in this study superimposed over bathymetry, contoured at 1000 m intervals, with depths shallower than 3000 m shaded. Dotted lines indicate the estimated mean locations of the Subantarctic and Polar Fronts of the Antarctic Circumpolar Current (ACC).

Time series of bottom pressure at the northern and southern moorings are shown in Figures 2a and 2b. Both show substantial variability on a variety of timescales.

The pressure gradient across Drake Passage can be interpreted using the geostrophic relationship $\rho_o f u = -\partial p/\partial y$. Integrating the geostrophic equation in the meridional direction shows that $\int_{y_S}^{y_N} f u \, dy = (p_N - p_S)/\rho_o$. Thus, at the depth of the bottom pressure gauges, transport per unit depth should be proportional to the pressure difference between the north and south sides of Drake Passage. Bottom pressure gauges are not calibrated precisely enough to estimate absolute geostrophic transport but can be used to infer temporal variability. Most variability in Drake Passage is believed to be barotropic [*Whitworth*, 1983], and assuming little baroclinic signal at the ocean floor, the bottom pressure difference across Drake Passage can be interpreted as an indicator of the barotropic transport. *Whitworth and Peterson* [1985] showed that fluctuations in total transport through Drake Passage were well correlated with fluctuations in bottom pressure difference, and in Parallel Ocean Climate Model results discussed in section 5, Drake Passage transport and bottom pressure difference have a correlation coefficient of 88%. Because of the rapid response of the barotropic mode, ACC transport through Drake Passage is conjectured to represent the entire circumpolar system [*Wearn and Baker*, 1980].

Figure 2c shows the bottom pressure difference across Drake Passage. The signal indicates substantial high-frequency fluctuations. *Hughes et al.* [1999] have suggested that bottom pressure at the north may be contaminated by the effects of the subtropical gyre so that southern bottom pressure will be a better proxy for transport fluctuations. This analysis considers the north BPR, the south BPR, and the differences between them.

3.2. Sea Surface Height

In contrast with the frequent measurements at a single location provided by bottom pressure recorders, the TOPEX/-Poseidon satellite measures sea surface height globally at 10 day intervals. For this study we have made use only of measurements from the TOPEX radar altimeter, which has lower noise levels than the Poseidon altimeter. Sea surface height measurements were used from all 127 ascending and 127 descending ground tracks for 171 cycles from September 1992 through May 1997, as shown in Figure 3. All of the standard data corrections were applied to the data, including the ocean tide, wet and dry tropospheric corrections, the ionospheric correction, solid earth tides, the pole tide, electro-

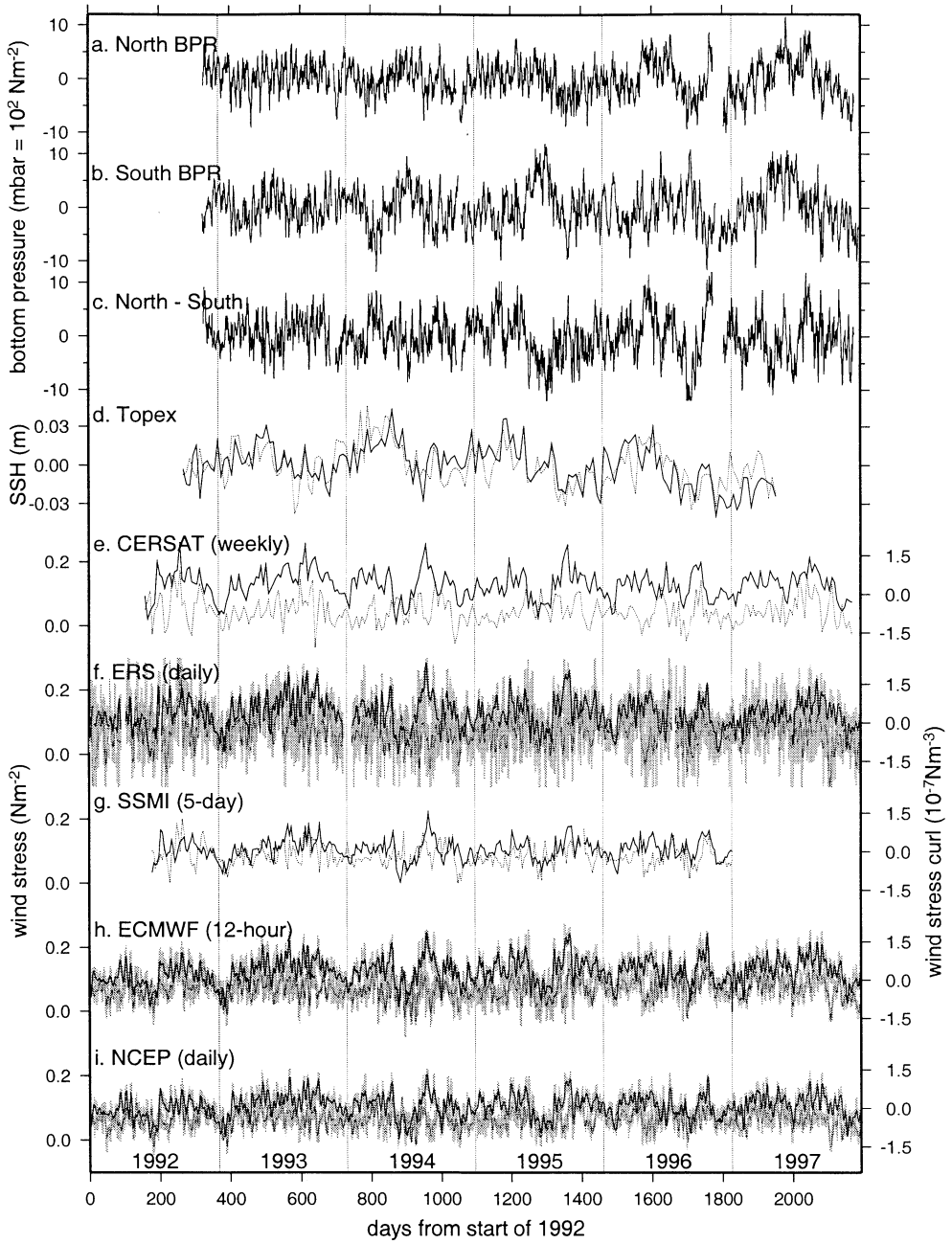

Figure 2. Time series of the data used in this study including (a) and (b) bottom pressure anomalies at the north and south moorings relative to their time mean, (c) the pressure difference between north and south moorings (again with a time mean removed), (d) sea surface height difference across the ACC from TOPEX altimeter ascending tracks (solid) and descending tracks (dotted), and (e)–(i) zonal wind stress (solid lines) and wind stress curl (dotted lines) averaged zonally around the globe and meridionally between 50°and 60°S, roughly corresponding to the latitude band of the ACC at Drake Passage. For the daily ERS winds, European Centre for Medium-Range Weather Forecasts (ECMWF) winds, and National Centers for Environmental Prediction (NCEP) winds, original data are shaded, and data filtered to retain only time periods longer than 10 days are solid.

magnetic bias, and inverse barometer correction. The time mean sea surface height was removed, and we worked with sea surface height anomalies.

Since we were specifically interested in the transport of the ACC rather than in height anomalies at fixed locations, we used the height anomaly difference across the ACC to determine geostrophic transport anomalies of the current. Height anomalies were determined by taking advantage of *Gille*'s [1994] iterative nonlinear jet-fitting procedure. This technique reconstructs the mean sea surface height across the ACC as well as providing a time series of height differences ($\Delta\eta$) relative to the mean. By design these estimates

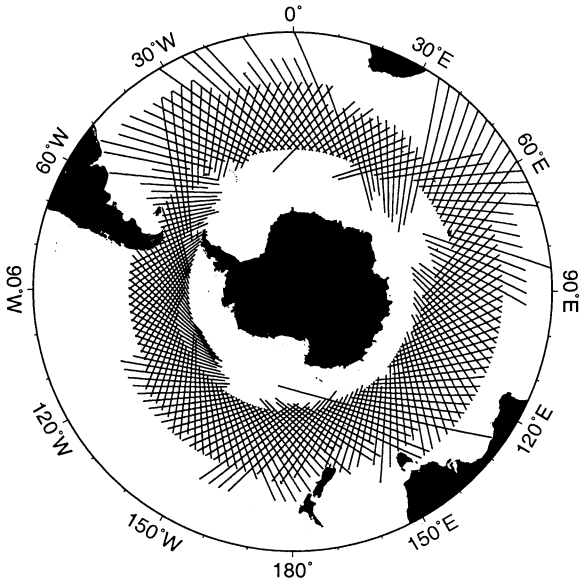

Figure 3. A total of 127 ascending and 127 descending TOPEX/Poseidon satellite tracks are spaced roughly 200 km apart in the Southern Ocean.

of $\Delta\eta$ represent the transport changes in the surface current but neglect effects due to rings or eddies that are not part of the Circumpolar Current transport.

In contrast with the bottom pressure, which indicates barotropic flow, sea surface height is expected to vary in response to local baroclinic effects as well as barotropic changes in ACC transport. Figure 2d shows the time series of zonally averaged sea surface height. Since the time sampling for each satellite ground track is slightly different, this zonally averaged record is determined by Fourier transforming the height information, phase shifting the data to account for the temporal sampling differences, and inverse transforming, before averaging ascending and descending tracks together.

The value of $\Delta\eta$ reaches a maximum in Southern Hemisphere fall. This appears analogous to the fall Δssh maximum found in the Gulf Stream, which has been attributed to upper ocean steric heating and is not expected to penetrate below the upper 250 m of the water column [*Stammer*, 1997a; *Kelly et al.*, 1999]. Despite their differing annual signals, when BPR differences and $\Delta\eta$ are filtered to retain frequencies longer than 20 days, they have a correlation coefficient of 22%, which is statistically significant above the 95% level.

3.3. Wind

Because of the lack of observing stations in the Southern Hemisphere, considerable doubts remain about the quality of winds over the ACC. This study considers five different wind products that each provide sufficiently long time series for comparison with the BPR and altimetric records. In each case, where wind stress was not directly available, 10 m winds were converted to wind stress using drag coefficients defined by *Large and Pond* [1982] with the modifications for low wind speeds adopted by *Mestas-Nuñez et al.* [1994].

The most promising method to measure winds over the global ocean is from satellite-borne scatterometers. By measuring radar backscatter off capillary waves on the ocean surface from multiple antennae, scatterometers collect information sufficient to help determine both wind speed and direction. The backscatter solution allows the possibility of up to four different wind directions. The most typical error is for the direction to be wrong by 180°, so additional information must often be supplied to determine the exact wind field. The scatterometers aboard ERS-1 and ERS-2 scan a single 500 km wide swath, and they have measured wind over the global ocean since August 1991. Two separate ERS wind products are considered in this study.

The Centre ERS d'Archivage et de Traitement (CERSAT) has produced weekly gridded maps of wind stress and wind stress curl from ERS scatterometer measurements. These maps are generated using a minimum variance method that is related to kriging [*Bentamy et al.*, 1996].

The ERS-1 and ERS-2 scatterometer swath patterns leave considerable spatial gaps that mapping schemes fill by interpolation. To minimize the impact of interpolation on short time periods, a daily wind product was prepared for this study. The Jet Propulsion Laboratory (JPL) has released raw wind vectors from ERS-1 and ERS-2 based on the work of *Freilich and Dunbar* [1993]. These were bin averaged at daily intervals and then zonally averaged with a 1° latitude window.

Another satellite instrument, the Special Sensor Microwave Imager (SSM/I), measures wind speed but not direction. SSM/I wind speeds were combined with wind directions from buoys and from ECMWF analysis using a variational analysis method [*Atlas et al.*, 1996]. This study uses the resulting wind fields, gridded at 0.5° by 5 day resolution [*Zlotnicki and Case*, 1998].

Wind fields generated by assimilating available observations into numerical atmospheric forecast models have also been used in this study. We employ the ECMWF Tropical Ocean–Global Atmosphere (TOGA) analysis winds gridded at 2.5° resolution [*Trenberth et al.*, 1989], which were also used by *Hughes et al.* [1999]. The winds come from an operational product used to initialize each forecast of the ECMWF model. They are generated by combining all available observations with the most recent numerical model prediction [*Andersson et al.*, 1998]. Wind observations include cloud winds, buoy measurements, and since 30 January 1996, scatterometer winds. SSM/I wind speeds are not used. In the Northern Hemisphere, ECMWF products incorporate measurements from numerous observing stations, but in the sparsely sampled Southern Hemisphere they are strongly influenced by satellite measurements including scatterometer winds (M. Miller, ECMWF, personal communication, 1998).

Finally, the NCEP reanalysis winds are used for the time period from 1992 to 1997. These winds are based on reanalysis of historical data using the updated NCEP atmospheric model [*Kalnay et al.*, 1996]. The reanalysis assimilates rawinsonde and cloud drift winds but does not currently include satellite winds from either SSM/I or scatterometry. Southern Hemisphere NCEP winds from 1979 to 1993 have well-documented errors, because surface pressure data were shifted 180° when they were assimilated. Only the first 4.5 months of this study are affected by this error, and results are not significantly different if these potentially erroneous dates are eliminated.

Time series of these wind products are shown in Figures 2e-i. All five wind products are closely correlated. In part this is true because CERSAT, JPL, and SSM/I wind products all use information from ECMWF to help interpret satellite wind products, while post-1996 ECMWF winds are generated by assimilating operational scatterometer winds. Although NCEP winds do not assimilate scatterometry, many of the other meteorological variables that they incorporate are also used by ECMWF. In principle, the satellite wind products should differ from ECMWF and NCEP most at high wavenumbers that are not resolved in these time series of zonally and meridionally averaged winds.

The NASA scatterometer (NSCAT), which provided 9 months of data from September 1996 through June 1997, scanned 600 km wide swaths on either side of the satellite ground track, providing better spatial and temporal coverage than the ERS scatterometer. However, the short duration of the NSCAT record is insufficient for comparison with the 5 year BPR and TOPEX records. In the CERSAT data products, for 9 months of overlapping data the correlation coefficient between zonally averaged NSCAT and ERS wind stresses is 93%, and the correlation coefficient for wind stress curls is 94%. JPL produced gridded NSCAT winds at the same time-space locations as SSM/I winds. Zonally averaged wind stresses from these series have a correlation coefficient of 95%, and zonally averaged wind stress curls have a correlation coefficient of 73%. All of these correlation coefficients are statistically significant at greater than the 99% level, suggesting that the zonally averaged products are consistent.

3.4. Annual and Semiannual Signals

The time series in Figure 2 appear to fluctuate on annual and semiannual frequencies. Because of the annual solar forcing of the Earth, all atmospheric and oceanic time series are likely to be coherent at the annual frequency, regardless of whether they are causally related [e.g., *Chelton*, 1982]. *Van Loon* [1967] reported that Southern Hemisphere winds have a strong semiannual cycle associated with differential cooling rates at different latitudes. In orer to eliminate false coherences the analysis in this paper begins by removing annual and semiannual cycles from the measurements.

Table 2 summarizes the characteristics of the annual and semiannual cycles removed from each time series. Together, the annual and semiannual cycles in the Southern Ocean account for a maximum of 25% of the variance in the data, though in most examples they are less significant.

The annual cycle is strongest in TOPEX measurements, most likely because of seasonal heating and cooling of the upper ocean. In contrast with the April maximum in TOPEX-derived $\Delta\eta$, the annual cycles of individual BPRs have maximum pressure in June, and the difference between them is greatest in February. The wind stress annual cycle reaches its maximum in July or August, during Southern Hemisphere winter. Wind stress curl is particularly noisy but has maxima for the annual cycle in winter months, between May and September. The large phase difference between transport and wind suggests that the annual cycles in these two time series might be due to independent processes.

Semiannual cycles of all the wind series indicate maximum amplitude in spring (March or April) and fall (September or October). The maximum in bottom pressure difference tends to be slightly later than the wind maxima, and TOPEX surface transport maxima appear later still (in April or May). The semiannual cycles in the individual BPRs indicate maximum amplitude at the end of June and the end of December, suggesting no close temporal link to the wind forcing.

Table 2. Amplitude and Phase of Annual and Semiannual Signals and the Percentage of the Total Variance (Once the Mean Has Been Removed) Explained by These Signals

Quantity	Annual		Semiannual		Percentage
	Amplitude	Phase, year day	Amplitude	Phase, year days	of Variance Explained, %
North BPR	1.6 mbar	151	0.9	173, 356	16
South BPR	1.9 mbar	175	1.5	181, 364	19
BPR Difference	0.7 mbar	54	0.8	100, 283	4
TOPEX (ascending)	0.010 m	109	0.003	113, 296	20
TOPEX (descending)	0.011 m	96	0.002	136, 319	25
CERSAT wind stress	$0.014\ \mathrm{Nm}^{-2}$	220	0.028	78, 260	25
CERSAT curl	$2.5\times10^{-8}\ \mathrm{Nm}^{-3}$	215	0.6×10^{-8}	69, 252	12
ERS wind stress	$0.016\ \mathrm{Nm}^{-2}$	224	0.025	82, 265	16
ERS curl	$1.03\times10^{-8}\ \mathrm{Nm}^{-3}$	147	1.01×10^{-8}	113, 296	1
SSM/I wind stress	$0.010\ \mathrm{Nm}^{-2}$	236	0.018	94, 276	19
SSM/I curl	$1.5\times10^{-8}\ \mathrm{Nm}^{-3}$	247	0.9×10^{-8}	95, 277	10
ECMWF wind stress	$0.012\ \mathrm{Nm}^{-2}$	208	0.023	86, 269	17
ECMWF curl	$0.45\times10^{-8}\ \mathrm{Nm}^{-3}$	236	1.15×10^{-8}	96, 278	3
NCEP wind stress	$0.004\ \mathrm{Nm}^{-2}$	202	0.020	87, 269	17
NCEP curl	$0.49\times10^{-8}\ \mathrm{Nm}^{-3}$	155	0.71×10^{-8}	103, 286	3

Phase is identified by the day of the year corresponding to maximum values. For ERS, ECMWF, and NCEP winds, results are shown for the unfiltered data (shading in Figure 2.) Results for the filtered data are essentially the same, though the fraction of variance explained is ~1% higher in each case.

4. Coherence of Wind and ACC Transport

The 5 year time series are intercompared using coherence analysis. Data are divided into 256 day segments that overlap by 128 days, a Hanning filter is applied, data are Fourier transformed, and coherences and phases are calculated according to (5) and (6). Since the time series have gaps and the data sets are sampled at different frequencies, error bars are estimated via Monte Carlo simulation. Each data time series is represented by 100 series of white noise with the same sampling gaps as the original data. The white noise series are segmented and filtered in the same way as the original data, coherences are calculated, and results are sorted. The fifth and 95th values are used to represent 5% and 95% confidence limits.

4.1. Bottom Pressure Difference Versus Wind Stress

Plate 1a shows the coherence between the bottom pressure difference across Drake Passage (Δp) and zonally averaged wind stress as a function of latitude for the five wind products. Since the wind products sample at different time intervals, the number of resolved frequencies differs. All five wind products indicate high coherence with Δp, particularly for winds between 55° and 60°S corresponding to the latitude range of Drake Passage. Winds show highest coherence with Δp at lower frequencies, corresponding to 40 or fewer cycles per year. Higher-frequency fluctuations are less likely to be well sampled in the available data records.

Coherences are considered significant if they exceed 0.51 for the SSM/I time series and 0.45 for all other wind products. Significance levels are largely determined by the length of the available time series, and the cutoff for the SSM/I time series is higher because 1997 winds were not available. If the measurements were pure white noise, 5.9% ± ~3.0% of frequency/latitude combinations would appear significant using the Monte Carlo test applied here. The first column of Table 3 summarizes the fraction of frequency/latitude combinations with statistically significant coherences between 50° and 62°S and between 1 and 18 cycles/256 days in Plate 1a. In most cases, the fraction of significant combinations exceeds 5.9% by more than 1 standard deviation; those that do not are footnoted. For all five wind stress products, more frequency/latitude combinations are statistically coherent than would be predicted from white noise. Except at the north BPR the three daily wind products (ERS, ECMWF, and NCEP) are coherent with bottom pressure at more frequency/latitude combinations than are the products representing longer time periods (CERSAT and SSM/I). This occurs largely because less frequent measurements have lower Nyquist frequencies, and coherences and phases are less well resolved near the Nyquist frequency. Thus, for this sort of analysis daily winds appear more useful than 5 day or weekly gridded winds. Surprisingly, NCEP winds, which assimilate no scatterometry, indicate the highest coherence with BPRs. Results computed from 365 day time segments (not shown) are qualitatively similar to those based on 256 day segments, but they are less statistically significant because fewer segments are available.

The corresponding phase lag of ACC transport relative to wind are shown in Plate 1b. Phase lags are meaningless when wind and bottom pressure are incoherent. When the time series are coherent (typically for low frequencies and wind stresses south of 50°S), bottom pressure tends to lag

Table 3. Percentage of Coherent Frequencies, Dominant Phase Lag Between Wind and Ocean, and Phase Lag variability

Product	Wind Stress			Wind Stress Curl		
	% Significant	Phase Lag	N/N_{TOT}	% Significant	Phase Lag	N/N_{TOT}
			Δ BPR ($\Delta p = p_N - p_S$)			
CERSAT	35	-35° ± 6°	43/182	12	-58° ± 19°	20/182
SSM/I	23	-6° ± 5°	72/336	9	74° ± 15°	22/336
ERS	41	-22° ± 3°	81/198	14	-40° ± 14°	26/180
ECMWF	42	-24° ± 5°	38/90	20	-37° ± 12°	18/90
NCEP	52	-16° ± 4°	66/126	12	-39° ± 18°	15/126
			South BPR ($-p_S$)			
CERSAT	28	-71° ± 6°	40/182	9	-69° ± 11°	15/182
SSM/I	25	12° ± 5°	76/336	9	92° ± 11°	26/336
ERS	52	-11° ± 3°	103/198	11	-78° ± 17°	19/180
ECMWF	56	-12° ± 3°	50/90	24	-45° ± 8°	22/90
NCEP	67	-8° ± 3°	85/126	21	-59° ± 13°	27/126
			North BPR (p_N)			
CERSAT	6[a]	-120° ± 39°	7/182	12	-155° ± 22°	22/182
SSM/I	5[a]	68° ± 17°	20/336	9	-68° ± 15°	27/336
ERS	4[a]	173° ± 26°	7/198	6[a]	-138° ± 25°	10/180
ECMWF	1[a]	162° ± ∞°	1/90	3[a]	-144° ± 12°	3/90
NCEP	6[a]	-107° ± 27°	8/126	4[a]	-142° ± 41°	5/126

For each of the bottom pressure products and each of the wind products, percentage of frequency/latitude combinations that are statistically coherent, median phase lag by which ocean lags wind at frequencies that are statistically coherent, and error about the median are given. Winds between 50° and 62°S are considered. For all wind products, fractions of variance explained are for frequencies from 1 to 18 cycles/256 days only. Phase relationships are for frequencies from 1 to 14 cycles/256 days for CERSAT and SSM/I (to avoid samples too close to the Nyquist frequency, where phase is poorly defined) and for frequencies from 1 to 18 cycles/256 days for ERS, ECMWF, and NCEP.

[a]Case where the percentage of significant combinations does not exceed 5.9% by more than one standard deviation.

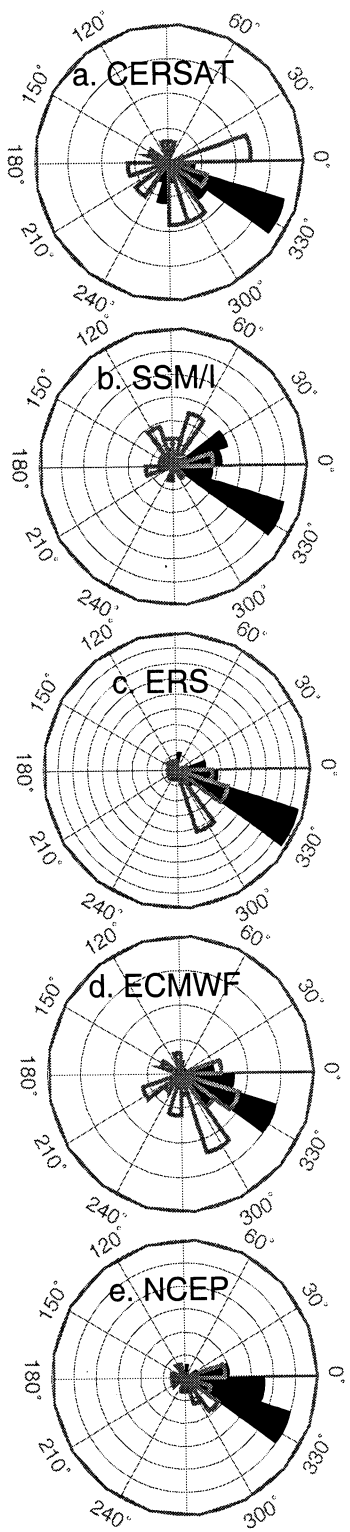

Figure 4. Rose histograms of statistically significant phases for each of the five wind products. Solid areas indicate wind stress, and open shaded regions indicate wind stress curl. To generate these plots, statistically significant latitude/frequency combinations are identified in the data for Plates 1a and 2a. The corresponding phases are identified in Plates 1b and 2b, and histograms are computed. Circular grid lines are at intervals of 5 samples for wind stress and 2.67 samples for wind stress curl. Wind latitudes and frequencies are the same as those used to compute median phase lags in Table 3.

wind stress by 0°–75°. This corresponds to less than a quarter cycle difference between wind and ACC transport.

What is the predominant phase lag between wind and ACC transport? Figure 4 shows histograms of phases for all frequency/latitude pairs that are statistically coherent. The BPR phase relative to wind stress (black regions) indicates that for all wind products, bottom pressure difference tends to lag wind stress between one eighteenth and one ninth of a cycle.

The third column of Table 3 lists the median phase lags and an estimate of the error in the median, which is determined by dividing the standard deviations about the median by $\sqrt{N}$. The number of points used to estimate the median phase lag, N, is listed in the fourth column along with the total number of frequency/latitude pairs considered for the median analysis, N_{TOT}. The median is shown rather than the mean because phase statistics are non-Gaussian and may be strongly biased by outliers. Since the initial choice of "branch cut" location can strongly influence the median, these calculations use a brute strength approach to find the median with the smallest possible standard deviation.

For the bottom pressure difference the median phase lag is ~20° for the daily ERS and ECMWF wind stresses but is slightly less for NCEP wind stress and is more variable for the less-frequently sampled SSM/I and CERSAT products. This corresponds to a typical phase lag of one eighteenth of a cycle. The errors in the median are consistently small enough that the medians can be considered nonzero.

If the ocean transport lagged the wind forcing by a fixed time interval, so that wind fluctuations were echoed by the ocean a fixed number of days later, then we would expect the phase lags plotted in Figure 4 to vary as a function of frequency, with longer lags for high-frequency events. Observations are not consistent with such a hypothesis but instead suggest that phase lag is constant as a function of frequency. For all wind stress products the standard deviation of phase, $<(\phi - \overline{\phi})^2>^{1/2}$, is about half the size of the standard deviation relative to a fixed time lag, $<(\phi - \phi(\overline{T}))^2>^{1/2}$, where $\overline{T}$ is the mean observed time lag and $\phi(\overline{T})$ is the corresponding phase lag.

Equation (10) predicted the phase lag between transport and wind for a system in which both a tendency term and linear bottom drag were present. The observed median phase lag of ~20° for wind stress indicates that $\tan(20°) \approx \omega/b$, suggesting that $b \approx 2.75\omega$. Thus the effective linear drag b appears to be frequency dependent rather than constant as *Wearn and Baker* [1980] assumed. Physically, this suggests that high-frequency fluctuations have greater drag or, in other words, that the ocean appears more viscous at high frequencies than at low frequencies. Although the physical processes may be unrelated, this could be thought of as a frequency domain analogue to biharmonic viscosity, which acts more strongly on high wavenumbers than on low wavenumbers.

4.2. Bottom Pressure Difference Versus Wind Stress Curl

As *Warren et al.* [1996] have pointed out, ACC transport may be more strongly influenced by wind stress curl than by wind stress. Plate 2a shows the coherence of wind stress

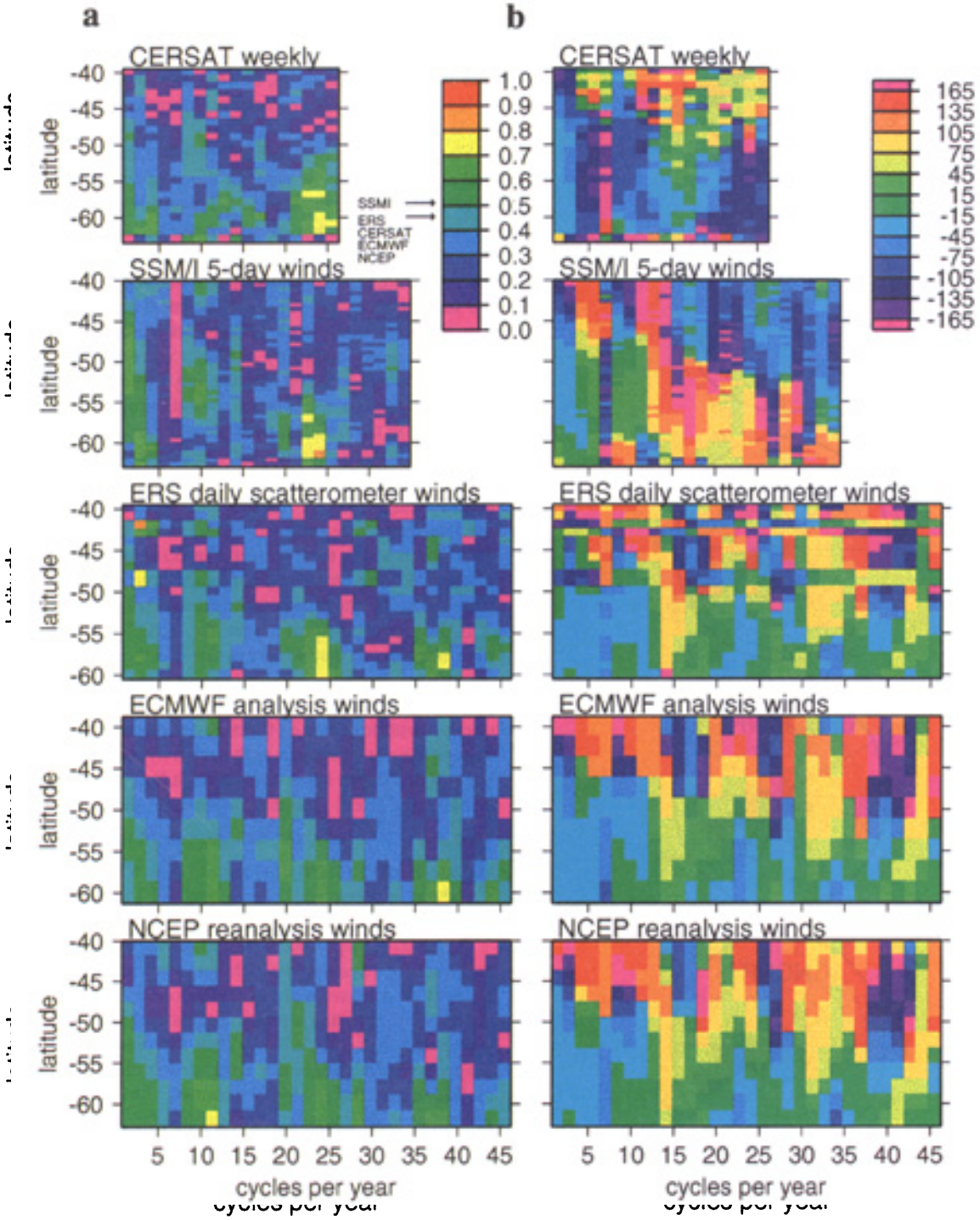

Plate 1. (a) Coherence between north–south bottom pressure difference and zonally averaged wind stress for each of five wind products. Winds vary as a function of latitude. The north–south pressure difference is a single time series from Drake Passage, a choke point of the ACC. Arrows on the scale indicate the value above which time series are coherent at the 95% significance level. (b) Phase of north–south bottom pressure difference relative to wind stress for each of five wind products.

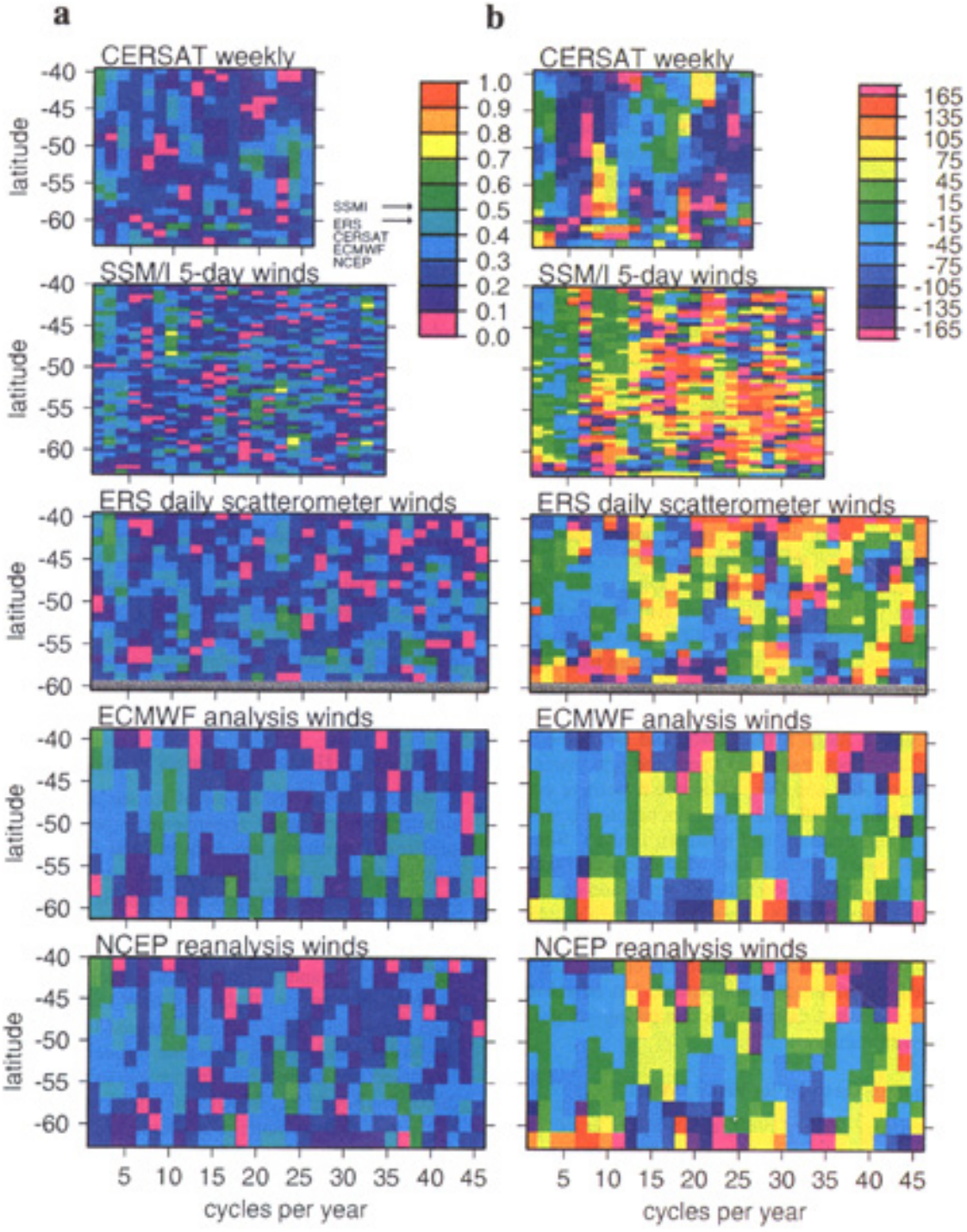

Plate 2. (a) Coherence between north–south bottom pressure difference and wind stress curl for each of five wind products, as in Plate 1a. (b) Phase of north–south bottom pressure difference relative to wind stress curl for each of five wind products.

curl with Δp. Coherences for wind stress curl are generally lower than those in Plate 1a, and this may be largely due to the elevated noise levels that arise from computing curl by differencing observed stresses. As in the comparisons of wind stress and Δp, the highest coherences occur at low frequencies. However, unlike wind stress, wind stress curl to the north of Drake Passage appears to be most coherent with transport through Drake Passage. The Sverdrup balance interpretation of the ACC requires that wind stress curl be negative, which is only observed south of ~50°S, in the latitude range where transport is less coherent with wind stress curl. This suggests that any impact that wind stress curl has on the temporal variability through Drake Passage may be an indirect effect associated with Sverdrup circulation set up in midlatitude closed basins rather than a direct Sverdrup forcing of the ACC. For comparison with wind stress results, Table 3 lists the fraction of frequency/latitude pairs at which curl and bottom pressure difference are statistically coherent.

For frequencies and latitudes where Δp and wind stress curl are statistically coherent, BPR difference across Drake Passage typically lags the wind curl as shown in Plate 2b. Open shaded regions in Figure 4 indicate rose histograms of BPR phase lag relative to wind stress curl. Typically, phase lags are between 0° and 90°, although the SSM/I winds suggest an entirely different relation. Similarly, the median phase lags in Table 3 indicate that typical phase lags are comparable to the median lags for wind stress but have much greater variations. As noted in section 2, a 0° phase lag between wind stress and BPR difference would provide a clear indication of a time-varying Sverdrup balance. The larger phase lags found here support the evidence that time-varying transport is not in simple Sverdrup balance.

In the latitude range between 40° and 60°S, the correlation coefficient between wind stress and wind stress curl varies between -0.3 and 0.3. (Maximum positive correlation occurs around 52°S, and maximum negative correlation is located at the northern and southern limits.) Since the coherence between transport and wind stress curl could be an artifact of the correlation between stress and curl, a second set of tests was done in which the portion of wind stress curl that is correlated with wind stress was removed. These tests (not shown) indicated marginally fewer statistically significant frequency/latitude combinations but otherwise resembled the coherence calculations comparing straight wind stress curl with transport.

4.3. South and North BPRs Versus Wind

As *Wearn and Baker* [1980] and *Hughes et al.* [1999] both noted, the northern and southern BPRs (p_N and p_S) have different variations and may respond differently to the wind. Table 3 indicates high coherence between p_S and wind stress. *Hughes et al.* [1999] have suggested that this high coherence occurs because the free mode barotropic response to wind fluctuations will follow contours of f/H, which are continuous (or nearly continuous) on the southern side of the Southern Ocean. Therefore they proposed that p_S may be a good proxy for ACC transport. The south BPR typically lags wind stress by ~10°, corresponding to one thirty-sixth of a cycle. This phase lag is less than what was found for Δp. Coherence analysis of the five wind products (not shown) indicates substantial phase differences between winds at 50° and 60°S. For the three lowest resolved frequencies, winds at 60°S lead winds at 55°–50°S by one thirty-sixth to one eighteenth of a cycle. Thus this reduced phase lag at the south BPR is consistent with p_S responding strongly to winds at 60°S.

Fluctuations in p_S are statistically coherent with wind stress curl at fewer frequency/latitude combinations, and the median phase lag is larger, corresponding to about one sixth of a cycle. SSM/I curl phases do not conform to phases from other wind products.

For p_N, Table 3 indicates no examples in which more frequency/latitude combinations are coherent with wind stress than would be expected for white noise. Therefore no definitive statement may be made about typical phase lags. For all wind stress curl products except NCEP, p_N is more often coherent with wind stress curl than with wind stress, suggesting that wind stress curl is more important in explaining what happens to the north side of Drake Passage than it is in explaining total transport fluctuations through Drake Passage. The north BPR trails wind stress curl with a median phase lag between 60° and 90°, slightly exceeding the lags found at the south BPR.

In contrast to p_S's link to ACC transport, *Hughes et al.* [1999] have speculated that p_N is highly sensitive to subtropical variability. If that is the case, then the higher sensitivity to wind stress curl at the north BPR suggests that a time-varying vorticity balance may establish itself in the subtropical basins. In contrast, the stronger response to wind stress than to wind stress curl at the south BPR may indicate that the circumpolar system itself is less strongly controlled by a classical Sverdrup balance.

4.4. TOPEX Height Differences Versus Wind

Altimetry provides a view of sea surface variability. Altimeter measurements are inherently noisier than bottom pressure, sampling is less frequent, and unlike bottom pressure, the sea surface height is likely to be influenced by surface-intensified eddy processes associated with baroclinic instability.

Coherence analysis is performed separately for each of the 127 ascending and 127 descending tracks. Since TOPEX samples once every 10 days, it only resolves fluctuations with frequencies less than the Nyquist frequency of 1 cycle/20 days, and unresolved higher-frequency variability may be aliased into the resolved frequency range [*Stammer et al.*, 2000; *Tierney et al.*, 2000]. In addition, daily winds are likely to match altimeter measurements more directly, with fewer aliasing problems. Table 4 summarizes the fraction of frequency/latitude combinations that are coherent with wind for all of the TOPEX ground tracks combined. Although the TOPEX samples are noisy, they provide an enormous number of observations, and in all cases, $\Delta\eta$ is more often coherent with wind than is expected for white noise. The fraction of coherent frequency/latitude pairs is comparable for wind stress and for wind stress curl, implying no clear distinction between momentum and vorticity dynamics in the upper ocean transport.

Figure 5 shows histograms of phases for each of the ma-

Table 4. Percentage of Coherent Frequencies, Dominant Phase Lag Between Wind and Ocean, and Phase Lag Variability for TOPEX Measurements and Wind

Product	Wind Stress			Wind Stress Curl		
	% Significant	Phase Lag	N	% Significant	Phase Lag	N
CERSAT	6.9	-111° ± 2°	1818	7.2	96° ± 2°	1898
SSM/I	7.7	-20° ± 2°	3764	6.8	-107° ± 2°	3316
ERS	7.3	-47° ± 2°	1640	7.2	147° ± 3°	1461
ECMWF	7.0	-61° ± 4°	707	7.6	161° ± 3°	771
NCEP	7.0	-71° ± 3°	989	7.4	163° ± 3°	1046

Coherence of sea surface height differences across the ACC from ascending and descending TOPEX measurements with wind products. For each wind product, columns indicate fraction of frequency/latitude combinations that are statistically coherent, median phase lag by which ocean lags wind at frequencies that are statistically coherent, estimated errors of the median, and the number of significant points, N. Winds between 50° and 62°S are considered. If the measurements were pure white noise, 5.9% ± ~0.2% of frequency/latitude combinations would appear significant using the Monte Carlo test applied here. All cases exceed 5.9% by more than one standard deviation. All results correspond to frequencies between 1 and 8 cycles/256 days only to reduce the influence of aliased unresolved variability at higher frequencies.

jor wind products, in analogy with Figure 4. In Table 4 the estimated errors of the median phase lags are small because errors are estimated by dividing the standard deviation about the median by $\sqrt{N}$, and N is large. The standard deviation of random phase samples evenly spaced between 0° and 360° would be 104°. Here in no case is the standard deviation about the median <90°. Thus these medians should be interpreted with caution. Although all five wind products indicate comparable fractions of coherent frequency/latitude pairs, the median phases for the daily winds (ERS, ECMWF, and NCEP) cluster more closely together.

Median phases of $\Delta\eta$ relative to wind stress in Table 4 are slightly larger than those found using BPR data. This suggests that surface transport lags wind stress by a larger time interval than bottom transport does. The low Nyquist frequency of the altimeter data means that phases are poorly resolved, and this may account for some of the phase shift. However, poor resolution of phases should increase the standard deviation of the measured phase without shifting the median phase. Therefore the large phase lag may be an indication that surface measurements represent a combination of a rapid barotropic mode and a slower baroclinic mode, while the deep BPRs see only the rapid barotropic mode.

Ascending and descending satellite tracks show different spatial patterns (not shown) in the coherence and phase of $\Delta\eta$ and wind. Although a longer time series might prove more revealing, the available altimeter data appear to be inadequate for identifying regions of particularly high coherence with wind. At the ocean surface, at any given location the variability of sea surface height is probably more strongly influenced by local phenomena, including local wind variations and baroclinic eddies, rather than zonally averaged winds.

5. Numerical Models

The results presented up to this point are based on observations. This section considers output from two ocean general circulation models, the Parallel Ocean Program (POP) [*Dukowicz and Smith*, 1994; *Maltrud et al.*, 1998] and the Parallel Ocean Climate Model (POCM 4C) [*Semtner and Chervin*, 1992; *Stammer et al.*, 1996].

Both POP and POCM are level models that have evolved from Bryan–Cox–Semtner formulations [*Bryan*, 1969; *Semtner*, 1974; *Cox*, 1984]. Although recent model developments have been independent, the models share many of the same newer features, including Richardson number dependent vertical mixing [*Pacanowski and Philander*, 1981] and free surfaces in place of the original rigid lid. The large-scale circulation patterns of these models display many similarities. The models differ in resolution, duration of run, surface heat and salt fluxes, and the degree to which the winds that drive them have been filtered in time and space. In addition, model output has been archived in different ways; by looking at results of both models we gain access to a broad range of physical quantities that have been saved at a variety of different frequencies. The large-scale circulation of these ocean models captures some major features of observed ocean circulation, as has been shown in intercomparisons between TOPEX/Poseidon altimeter measurements and upper ocean model output from POCM [*Stammer et al.*, 1996; *McClean et al.*, 1997] and from POP [*Fu and Smith*, 1996; *McClean et al.*, 1997]. However, results of eddy-permitting model runs are sensitive to model resolution and horizonal viscosity, and a 0.1° resolution version of POP for the North Atlantic appears to be more realistic than the coarser-resolution models considered here [*Smith et al.*, 2000]

The POP model, developed at Los Alamos National Laboratory, ran with 0.28° zonal by 0.28cos([lat])° meridional resolution with 20 vertical levels [*Dukowicz and Smith*, 1994; *Maltrud et al.*, 1998]. POP was distinguished by using unsmoothed bottom topography and an implicit free surface in which the air-sea interface can evolve freely. After an initial spin up, POP ran for three consecutive 10 year time periods. This study uses the second and third 10 year periods, which are identified as run 7 and run 11, respectively, by *Maltrud et al.* [1998]. Both were driven by 3-day averaged ECMWF

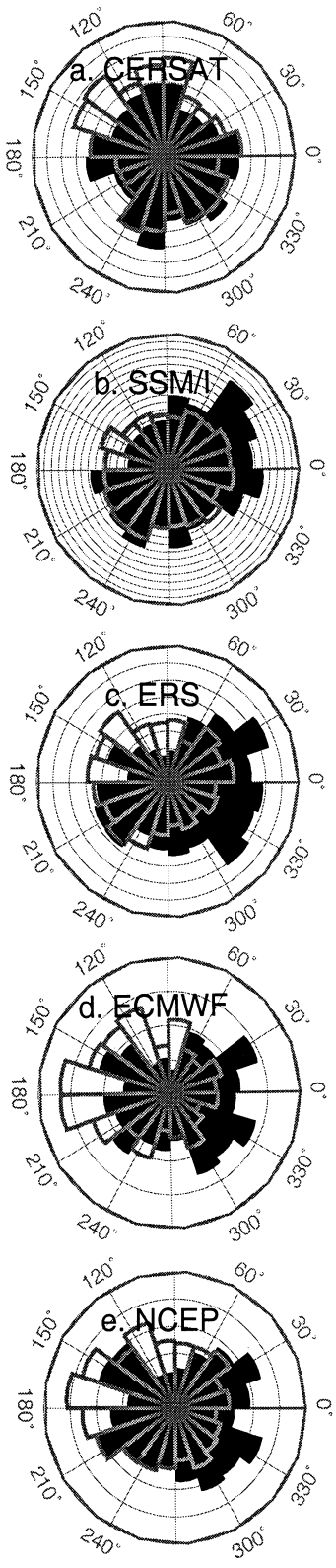

Figure 5. Rose histograms of statistically significant phases for TOPEX altimeter measurements versus each of the five wind products. Data are generated as in Figure 4. Circular grid lines are at intervals of 20 samples for both wind stress and wind stress curl.

Table 5. Percentage of Coherent Frequencies, Dominant Phase Lag Between Wind and Ocean, and Phase Lag Variability for GCM Output and Wind

	Wind Stress		Wind Stress Curl	
	% Significant	Phase Lag	% Significant	Phase Lag
	POP [Maltrud et al., 1998]			
Run 7	79	-10°± 2°	56	-8°± 3°
Run 11	83	-13°± 2°	63	-4°± 3°
	POCM [Semtner and Chervin, 1992]			
p_N	31	-25°± 7°	23	-22°± 17°
$-p_S$	76	-1°± 2°	78	5°± 4°
Δp	76	-8°± 2°	57	-4°± 6°
T	81	-6°± 2°	63	2°± 5°

Coherence of Drake Passage transport and bottom pressure difference with model wind forcing. Shown are the fraction of frequency/latitude combinations that are statistically coherent, median phase lag by which ocean lags wind, and estimated errors in the median. In all cases, the percentage of statistically significant coherences exceeds 5.9% by more than 1 standard deviation. Percentages of coherent points and median phase lags are for frequencies between 1 and 18 cycles/256 days and winds at 2.5° intervals from 50° to 60°S.

analysis winds from 1985 to 1995. In run 7, temperature and salinity were restored to seasonal climatology [*Levitus*, 1982], while run 11 used seasonal heat fluxes from *Barnier et al.* [1995]. *Best et al.* [1999] discuss Southern Ocean eddies in POP. Time series of Drake Passage transport are highly correlated in runs 7 and 11 and indicate substantial interannual variability [*Maltrud et al.*, 1998, Figures 1 and 2].

POCM is an outgrowth of a global model set up by *Semtner and Chervin* [1992]. It ran with 0.4° zonal by 0.4 cos([lat])° meridional resolution and 20 vertical levels and used a free surface described by *Killworth et al.* [1991]. POCM 4C, used in this study, was forced with ECMWF reanalysis winds and with heat and freshwater fluxes based on ECMWF reanalysis from 1979 through 1993. (Starting in 1994, POCM 4C was forced with operational winds, operational heat fluxes, and "climatological" freshwater fluxes.) All forcing fields were determined by interpolating between 3 day updates. Details of the Southern Ocean dynamical balance in an earlier version of this model are discussed by *Gille* [1997]. Figure 6 shows the time series of Drake Passage transport, bottom pressure, and winds used in this study. Model bottom pressure increases steadily over the course of the model run as the model continues to spin up, but the mean bottom pressure difference remains nearly constant. Model transport exceeds observational estimates of Drake Passage transport by $\sim 30 \times 10^6$ m^3 s^{-1}; this might be attributed to a number of factors including coarse representation of bathymetry or the choice of model viscosity.

General circulation model (GCM) transport, bottom pressure, and wind fields were preprocessed in the same way as the observations discussed in section 3. Like the results from BPRs in Plates 1 and 2, transport and bottom pressure in both GCMs are most coherent with wind stress at latitudes within Drake Passage and at frequencies $<\sim$ 1 cycle/10 days. Co-

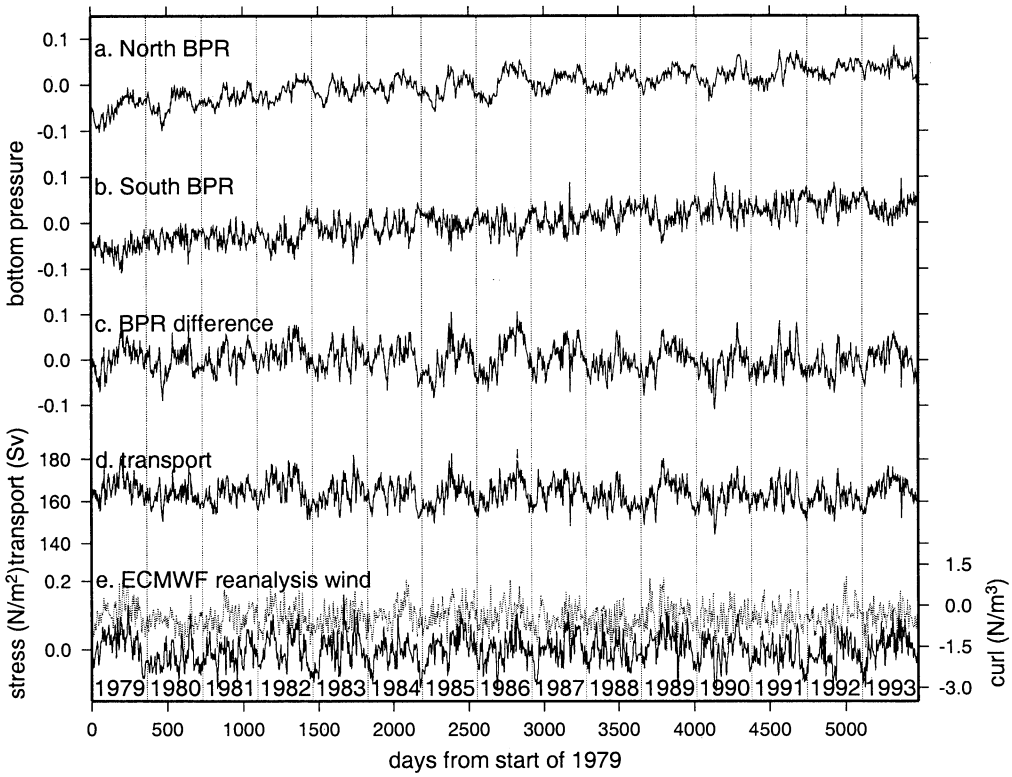

Figure 6. Time series of the output from the Parallel Ocean Climate Model (POCM 4C) run including (a) bottom pressure on the north side of Drake Passage, (b) south bottom pressure, (c) bottom pressure difference, (d) Drake Passage transport, and (e) zonal wind stress (solid lines) and wind stress curl (dotted lines) from ECMWF reanalysis, averaged zonally around the globe and meridionally between 50° and 60°S.

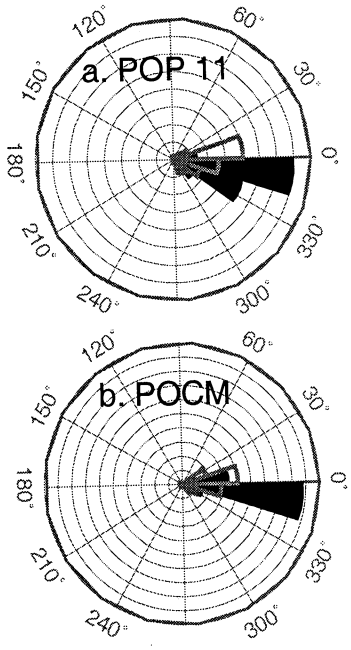

Figure 7. Rose histograms of statistically significant phases for Drake Passage transport in the Parallel Ocean Program (POP) and POCM, compared with ECMWF winds between 50° and 60°S, at frequencies from 1 to 18 cycles/256 days. Solid regions indicate wind stress, and shaded regions indicate wind stress curl. Concentric grid lines are at intervals of 5 units for both stress and curl.

herence with wind stress curl is greatest for winds north of Drake Passage. Table 5 indicates that the fraction of statistically coherent frequency/latitude combinations is greater for GCM output than for BPR observations. This probably results from the lower noise levels in the numerical model output than in the observations.

Figure 7 shows phases of statistically significant frequency/latitude pairs. These results indicate that compared with observations, numerical model transports lag winds by smaller frequency intervals. Table 5 summarizes the median phase lags for various model transport and bottom pressure quantities compared with ECMWF winds. As the BPRs also indicated, model p_N lags the wind by more than Δp, and model p_S varies almost simultaneously with the winds. POP phase lags appear larger than POCM phase lags; this might result from POP's higher resolution or longer initial spin-up, particularly for run 11. In contrast with the BPR phase lags, model results are less clearly represented by assuming a constant frequency lag: the standard deviation of model transports about a mean phase $<(\phi - \overline{\phi})^2>^{1/2}$ is about the same as the standard deviation about a mean time lag $<(\phi - \phi(\overline{T}))^2>^{1/2}$. This could be a result of the near-zero phase lag in the BPR record, or it may indicate that model phase lags vary substantially with frequency.

On the basis of the phase relationship (10) these results suggest that in the models the effective bottom drag may exceed its real ocean values. To maintain numerical stability, both POP and POCM rely on relatively large viscosity,

which may be responsible for the reduced model phase lag. The median phase lag of the model output is between 30 and 80% of the median phase lag in the observations. Assuming that linear drag can be approximated as biharmonic diffusion $b \approx \nu/L_H^4$, these results suggest that numerical model viscosity might be 1.2–3 times too large. Further tests would be required to demonstrate whether numerical model phase lag can be tuned by adjusting viscosity or whether other processes are responsible for controlling model phase lag.

6. Summary

This study has examined how ACC transport responds to variations in wind forcing using five different wind products. Results show strong annual and semiannual cycles in winds as well as in transport estimates from altimetry and from BPRs on either side of Drake Passage. The annual cycle of altimeter data shows an April surface transport maximum, which is consistent with fall maxima seen in altimetric records for the Gulf Stream and the Kuroshio. This surface annual cycle is out of phase with the wind and is not duplicated by the 1000 m deep BPRs, suggesting that steric heating dominates the signal.

Both altimeter estimates and BPR estimates are used as proxies for Drake Passage transport. Both show statistically significant coherence with all five wind products. The highest coherences occur for winds in the latitude of Drake Passage, between 55° and 60°S, at frequencies lower than ~1 cycle/10 days. Coherences between wind and bottom pressure on the south side of Drake Passage are slightly larger than coherences between wind and Δp, as *Hughes et al.* [1999] also reported. For all five wind products, phase lags show wind leading ocean transport by a fixed frequency interval of about one eighteenth of a cycle for bottom pressure difference and about one sixth of a cycle for surface transport from altimetry. This suggests that ocean response to wind stress represents a combination of instantaneous response due to frictional or nonlinear effects and quarter cycle time-delayed effects due to the tendency term. The ocean GCMs, POP and POCM, both duplicate the spatial patterns of high coherence at low frequencies and in the latitudes of Drake Passage. However, the model transports vary in tandem with the winds, allowing almost no phase lag. This might be due to the high viscosity of the numerical models.

Compared with wind stress, wind stress curl is less statistically coherent with Drake Passage transport, and phase lags between wind and bottom pressure are larger. This may result from wind stress curl's higher noise levels compared to wind stress, but it may also imply that time-varying Sverdrup-type vorticity balances are not established in the latitudes of the ACC. In both GCM output and observations, highest coherences with wind stress curl occur for winds north of Drake Passage. In these regions, positive wind stress curls can drive Sverdrup circulation within the subtropical gyres that may indirectly force the ACC, but positive curl cannot drive the southward spiraling flow toward Drake Passage. In the latitudes of Drake Passage, wind stress is coherent with ACC transport and is therefore likely to govern ACC transport fluctuations.

Acknowledgments. We are grateful to John Green, Chris Hughes, and Mike Meredith for helpful discussion and to Phil Woodworth, Ian Vassie, and Kate Grose for making their bottom pressure data readily available, both in preliminary form and publicly via anonymous ftp. Mat Maltrud and Rick Smith provided output from the POP model. Bert Semtner was responsible for the POCM model runs. Wind data were provided by the French data processing facility CERSAT, by JPL's PO/DAAC (SSM/I and raw ERS vectors), by the NOAA-CIRES Climate Diagnostics Center, Boulder, Colorado (http://www.cdc.noaa.gov/ (NCEP)), and by the National Center for Atmospheric Research (NCAR). NCAR provided computational resources to extract ECMWF wind fields through a seed grant for new faculty. Rex Gibson and Keith Fielding of ECMWF and Joey Comeaux of NCAR answered questions about the ECMWF winds. Wesley Ebisuzaki of NOAA provided similar help with the NCEP winds. Comments from Peter Gent, Steve Rintoul, and Frédéric Vivier have improved this presentation. STG was funded by the North Atlantic Treaty Organization under a grant awarded in 1997 and by JPL contract 960875 with Scripps Institution of Oceanography.

References

Andersson, E., et al., The ECMWF implemention of three dimensional variational assimilation (3D-Var), III: Experimental results, *Q. J. R. Meteorol. Soc.*, *124*, 1831–1860, 1998.

Atlas, R., R. N. Hoffman, S. C. Bloom, J. C. Jusem, and J. Ardizzone, A multiyear global surface wind velocity dataset using SSM/I wind observations, *Bull. Am. Meteorol. Soc.*, *77*, 869–882, 1996.

Baker, D. J., Jr., A note on Sverdrup balance in the Southern Ocean, *J. Mar. Res.*, *40S*, 21–26, 1982.

Barnier, B., L. Siefridt, and P. Marchesiello, Thermal forcing for a global ocean circulation model using a three-year climatology of ECMWF analyses, *J. Mar. Syst.*, *6*, 363–380, 1995.

Bentamy, A., N. Grima, Y. Quilfen, V. Harscoat, C. Maroni, and S. Pouliquen, An atlas of surface wind from ERS-1 scatterometer measurements, tech. rep., 229 pp., French Res. Inst. for the Exploit. of the Sea, Plouzané, France, 1996.

Best, S. E., V. O. Ivchenko, K. J. Richards, R. D. Smith, and R. C. Malone, Eddies in numerical models of the Antarctic Circumpolar Current and their influence on the mean flow, *J. Phys. Oceanogr.*, *29*, 328–350, 1999.

Bryan, K., A numerical method for the study of the circulation of the world ocean, *J. Comput. Phys.*, *1*, 119–143, 1969.

Cai, W., and P. G. Baines, Interactions between thermohaline and wind-driven circulations and their relevance to the dynamics of the Antarctic Circumpolar Current, in a coarse-resolution global ocean general circulation model, *J. Geophys. Res.*, *101*, 14,073–14,093, 1996.

Chelton, D. B., Statistical reliability and the seasonal cycle: Comments on "Bottom pressure measurements across the Antarctic Circumpolar Current and their relation to the wind," *Deep Sea Res., Part A*, *29*, 1381–1388, 1982.

Cox, M. D., A primitive equation 3-dimensional model of the ocean, *GFDL Ocean Group Tech. Rep. 1*, 143 pp. Geophys. Fluid Dyn. Lab./Natl. Oceanic and Atmos. Admin., Princeton Univ., Princeton, N.J., 1984.

Dukowicz, J. K., and R. D. Smith, Implicit free-surface method for the Bryan–Cox–Semtner ocean model, *J. Geophys. Res.*, *99*, 7991–8014, 1994.

Freilich, M. H., and R. S. Dunbar, A preliminary C-band scatterometer model function for the ERS-1 AMI instrument, in *Proceedings First ERS-1 Symposium: Space at the Service of Our Environment, Cannes, France, ESA Spec. Publ., SP-359*, 79–84, 1993.

Fu, L. L., and R. D. Smith, Global ocean circulation from satellite altimetry and high-resolution computer simulation, *Bull. Am. Meteorol. Soc.*, *77*, 2625–2636, 1996.

Gent, P. R., W. G. Large, and F. O. Bryan, What sets the mean

transport through Drake Passage?, *J. Geophys. Res.*, this issue.
Gille, S. T., Mean sea surface height of the Antarctic Circumpolar Current from Geosat data: Method and application, *J. Geophys. Res.*, *99*, 18,255–18,273, 1994.
Gille, S. T., The Southern Ocean momentum balance: Evidence for topographic effects from numerical model output and altimeter data, *J. Phys. Oceanogr.*, *27*, 2219–2232, 1997.
Gille, S. T., Evaluating Southern Ocean response to wind forcing, *Phys. Chem. Earth*, *24*, 423–428, 1999.
Gnanadesikan, A., and R. W. Hallberg, On the relationship of the Circumpolar Current to Southern Hemisphere winds in large-scale ocean models, *J. Phys. Oceanogr.*, in press, 2000.
Hughes, C. W., On the obscurantist physics of "form drag" in theorizing about the Circumpolar Current: Comments, *J. Phys. Oceangr.*, *27*, 209–210, 1997.
Hughes, C. W., M. P. Meredith, and K. J. Heywood, Wind driven transport fluctuations through Drake Passage: A southern mode, *J. Phys. Oceangr.*, *29*, 1971–1992, 1999.
Johnson, G. C., and H. L. Bryden, On the size of the Antarctic Circumpolar Current, *Deep Sea Res., Part A*, *36*, 39–53, 1989.
Kalnay, E., et al., The NCEP/NCAR 40-year reanalysis project, *Bull. Am. Meteorol. Soc.*, *77*, 437–471, 1996.
Kelly, K. A., S. Singh, and R. X. Huang, Seasonal variations of sea surface height in the Gulf Stream region, *J. Phys. Oceanogr.*, *29*, 313–327, 1999.
Killworth, P. D., D. Stainforth, D. J. Webb, and S. M. Paterson, The development of a free-surface Bryan-Cox-Semtner ocean model, *J. Phys. Oceanogr.*, *21*, 1331–1348, 1991.
Large, W. G., and S. Pond, Sensible and latent heat flux measurements over the ocean, *J. Phys. Oceanogr.*, *12*, 464–482, 1982.
Levitus, S., Climatological atlas of the world oceans, *Prof. Paper 13*, 173 pp., Natl. Oceanic and Atmos. Admin., Princeton, N.J., 1982.
Maltrud, M. E., R. D. Smith, A. J. Semtner, and R. C. Malone, Global eddy-resolving ocean simulations driven by 1985-1994 atmospheric winds, *J. Geophys. Res.*, *103*, 30,825–30,853, 1998.
Marshall, D., Topographic steering of the Antarctic Circumpolar Current, *J. Phys. Oceanogr.*, *25*, 1636–1650, 1995.
McClean, J. L., A. J. Semtner, and V. Zlotnicki, Comparisons of mesoscale variability in the Semtner-Chervin 1/4° model, the Los Alamos Parallel Ocean Program 1/6° model, and TOPEX/Poseidon data, *J. Geophys. Res.*, *102*, 25,203–25,226, 1997.
Meredith, M. P., J. M. Vassie, K. J. Heywood, and R. Spencer, On the temporal variability of the transport through Drake Passage, *J. Geophys. Res.*, *101*, 22,485–22,494, 1996.
Mestas-Nuñez, A. M., D. B. Chelton, M. H. Freilich, and J. G. Richman, An evaluation of ECMWF-based climatological wind stress fields, *J. Phys. Oceanogr.*, *24*, 1532–1549, 1994.
Munk, W. H., and E. Palmén, Note on the dynamics of the Antarctic Circumpolar Current, *Tellus*, *3*, 53–55, 1951.
Nowlin, W. D., Jr., and J. M. Klinck, The physics of the Antarctic Circumpolar Current, *Rev. Geophys.*, *24*, 469–491, 1986.
Olbers, D., Comments on "On the obscurantist physics of 'form drag' in theorizing about the Circumpolar Current," *J. Phys. Oceanogr.*, *28*, 1647–1654, 1998.
Pacanowski, R. C., and S. G. H. Philander, Parameterization of vertical mixing in numerical models of tropical oceans, *J. Phys. Oceanogr.*, *11*, 1443–1451, 1981.
Peterson, R. G., On the transport of the Antarctic Circumpolar Current through Drake Passage and its relation to wind, *J. Geophys. Res.*, *93*, 13,993–14,004, 1988.
Semtner, A. J., A general circulation model for the world ocean, Tech. Rep. 9, 99 pp., Univ. of Calif., Los Angeles, 1974.
Semtner, A. J., and R. M. Chervin, Ocean general circulation from a global eddy-resolving model, *J. Geophys. Res.*, *97*, 5493–5550, 1992.
Smith, R. D., M. E. Maltrud, F. O. Bryan, and M. W. Hecht, Numerical simulation of the North Atlantic at 1/10°, *J. Phys. Oceanogr.*, in press, 2000.
Stammer, D., Global characteristics of ocean variability estimated from regional TOPEX/Poseidon altimeter measurements, *J. Phys. Oceanog.*, *27*, 1743–1769, 1997a.
Stammer, D., Steric and wind-induced changes in TOPEX/Poseidon large-scale sea surface topography observations, *J. Geophys. Res.*, *102*, 20,987–21,009, 1997b.
Stammer, D., R. Tokmakian, A. Semtner, and C. Wunsch, How well does a 1/4° global ciculation model simulate large-scale oceanic observations?, *J. Geophys. Res.*, *101*, 25,779–25,811, 1996.
Stammer, D., C. Wunsch, and R. M. Ponte, De-aliasing of global high frequency barotropic motions in altimeter observations, *Geophys. Res. Lett.*, *27*, 1175–1178, 2000.
Stevens, D. P., and V. O. Ivchenko, The zonal momentum balance in a realistic eddy resolving general circulation model of the Southern Ocean, *Q. J. R. Meteorol. Soc.*, *123*, 929–951, 1997.
Stommel, H., A survey of ocean current theory, *Deep Sea Res.*, *4*, 149–184, 1957.
Trenberth, K. E., J. G. Olson, and W. G. Large, A global ocean wind stress climatology based on ECMWF analyses, *Tech. Rep. NCAR/TN-338+STR*, 93 pp., Natl. Cent. for Atmos. Res., Boulder, Colo., 1989.
Tierney, C., J. Wahr, F. Bryan, and V. Zlotnicki, Short-period oceanic circulation: implications for satellite altimetry, *Geophys. Res. Lett.*, **27**, 1255-1258, 2000.
van Loon, H., The half-yearly oscillations in middle and high southern latitudes and the coreless winter, *J. Atmos. Sci.*, *24*, 472–486, 1967.
Völker, C., Momentum balance in zonal flows and resonance of baroclinic Rossby waves, *J. Phys. Oceanogr.*, *29*, 1666–1681, 1999.
Warren, B. A., J. H. LaCasce, and P. E. Robbins, On the obscurantist physics of "form drag" in theorizing about the Circumpolar Current, *J. Phys. Oceanogr.*, *26*, 2297–2301, 1996.
Warren, B. A., J. H. LaCasce, and P. E. Robbins, On the obscurantist physics of "form drag" in theorizing about the Circumpolar Current: Reply, *J. Phys. Oceanogr.*, *27*, 211–212, 1997.
Warren, B. A., J. H. LaCasce, and P. E. Robbins, Comments on "On the obscurantist physics of 'form drag' in theorizing about the Circumpolar Current": Reply, *J. Phys. Oceanogr.*, *28*, 1655–1658, 1998.
Wearn, R. B., Jr., and D. J. Baker, Jr., Bottom pressure measurements across the Antarctic Circumpolar Current and their relation to the wind, *Deep Sea Res., Part A*, *27*, 875–888, 1980.
Whitworth, T., III, Monitoring the transport of the Antarctic Circumpolar Current at Drake Passage, *J. Phys. Oceanogr.*, *13*, 2045–2057, 1983.
Whitworth, T., III, and R. G. Peterson, Volume transport of the Antarctic Circumpolar Current from bottom pressure measurements, *J. Phys. Oceanogr.*, *15*, 810–816, 1985.
Wunsch, C., The work done by the wind on the oceanic general circulation, *J. Phys. Oceanogr.*, *28*, 2332–2340, 1998.
Zlotnicki, V., and K. Case, Atlas and Ardizzone SSMI-derived winds, version 2, PO-DAAC gridding, *DMSP-SSM/I and ADEOS-NSCAT Mean Wind Fields* [CD-ROM], PO.DAAC Distrib. Active Arch. Cent., Jet Propul. Lab., Calif. Inst. of Technol., Pasadena, 1998.

S. T. Gille, Department of Earth System Science, University of California, Irvine, CA 92697-3100. (sgille@uci.edu)
K. J. Heywood, School of Environmental Sciences, University of East Anglia, Norwich NR4 7TJ, England, U.K.
D. P. Stevens, School of Mathematics, University of East Anglia, Norwich NR4 7TJ, England, U.K.
R. T. Tokmakian, Department of Oceanography, Naval Postgraduate School, Monterey, CA 93943.

(Received May 3, 1999; revised October 19, 1999;
accepted December 9, 1999.)